

1 **Title**

2 Developmental, cellular, and biochemical basis of transparency in the glasswing butterfly

3 *Greta oto*

4

5 **Authors**

6 Aaron F. Pomerantz^{1,2*}, Radwanul H. Siddique^{3,4}, Elizabeth I. Cash⁵, Yuriko Kishi^{6,7},

7 Charline Pinna⁸, Kasia Hammar², Doris Gomez⁹, Marianne Elias⁸, Nipam H. Patel^{1,2,6*}

8

9 **Affiliations**

10 ^{1.} Department Integrative Biology, University of California Berkeley, Berkeley, CA
11 94720.

12 ^{2.} Marine Biological Laboratory, Woods Hole, MA 02543.

13 ^{3.} Image Sensor Lab, Samsung Semiconductor, Inc., 2 N Lake Ave. Ste. 240, Pasadena,
14 CA 91101, USA.

15 ^{4.} Department of Medical Engineering, California Institute of Technology, Pasadena, CA
16 91125.

17 ^{5.} Department of Environmental Science, Policy, & Management University of California,
18 Berkeley, Berkeley, CA 94720.

19 ^{6.} Department Molecular Cell Biology, University of California Berkeley, Berkeley, CA
20 94720.

21 ^{7.} Department of Biology and Biological Engineering, California Institute of Technology,
22 Pasadena, CA.

23 ^{8.} ISYEB, 45 rue Buffon, CP50, Paris, CNRS, MNHN, Sorbonne Université, EPHE,
24 Université des Antilles, France.

25 ^{9.} CEFE, 1919 route de Mende, Montpellier, CNRS, Univ Montpellier, Univ Paul Valéry
26 Montpellier 3, EPHE, IRD, France.

27

28 * **Corresponding author.** Email: pomerantz_aaron@berkeley.edu, npatel@mbl.edu

29 **Abstract (150 words)**

30 Numerous species of Lepidoptera have transparent wings, which often possess scales
31 of altered morphology and reduced size, and the presence of membrane surface
32 nanostructures that dramatically reduce reflection. Optical properties and anti-
33 reflective nanostructures have been characterized for several ‘clearwing’ Lepidoptera,
34 but the developmental basis of wing transparency is unknown. We apply confocal and
35 electron microscopy to create a developmental time-series in the glasswing butterfly,
36 *Greta oto*, comparing transparent and non-transparent wing regions. We find that
37 scale precursor cell density is reduced in transparent regions, and cytoskeletal
38 organization differs between flat scales in opaque regions, and thin, bristle-like scales
39 in transparent regions. We also reveal that sub-wavelength nanopillars on the wing
40 membrane are wax-based, derive from wing epithelial cells and their associated
41 microvillar projections, and demonstrate their role in enhancing-anti-reflective
42 properties. These findings provide insight into morphogenesis of naturally organized
43 micro- and nanostructures and may provide bioinspiration for new anti-reflective
44 materials.

45 **Introduction**

46 The wings of butterflies and moths (Lepidoptera) have inspired studies across a variety of
47 scientific fields, including evolutionary biology, ecology, and biophysics (1–3).

48 Lepidopteran wings are generally covered with rows of flat, partially overlapping scales
49 that endow the wings with colorful patterns. Adult scales are chitin-covered projections
50 that serve as the unit of color for the wing. Each scale can generate color through
51 pigmentation via molecules that selectively absorb certain wavelengths of light, structural
52 coloration, which results from light interacting with the physical nanoarchitecture of the
53 scale, or a combination of both pigmentary and structural coloration (4, 5). Cytoskeletal
54 dynamics, including highly organized F-actin filaments during scale cell development,
55 play essential roles in wing scale elongation and prefigure aspects of scale ultrastructure
56 (6, 7).

57 In contrast to typical colorful wings, numerous species of butterflies and moths
58 possess transparent wings that allow light to pass through, so that objects behind them can
59 be distinctly seen (Fig. 1A-H, 8–10). This trait has been interpreted as an adaptation in the
60 context of camouflage, in which some lineages evolved transparent wings as crypsis to
61 reduce predation (11–13). Transparency results from the transmission of light across the
62 visible spectrum through a material, in this case the chitin membrane, without appreciable
63 absorption or reflection. Levels of reflection are largely determined by the differences in
64 refractive indices between biological tissues and the medium, and a larger difference
65 results in higher surface reflection. Our knowledge on mechanisms underlying
66 transparency in nature is primarily from aquatic organisms, which are frequently
67 transparent, aided by the close match between the refractive indices of their aqueous
68 tissue and the surrounding media — water (14). By contrast, transparency is rare and
69 more challenging to achieve on land, primarily due to the large difference between the

70 refractive indices of terrestrial organism's tissue ($n = \sim 1.3-1.5$) and air ($n = 1$), which
71 results in significant surface reflection (9, 15, 16).

72 Nevertheless, some organisms have evolved morphological innovations that
73 overcome the challenges of terrestrial transparency, notably in the form of anti-reflective
74 nanostructures. Early studies elucidated highly-ordered sub-wavelength nanostructures
75 (termed 'nipple arrays') on the corneal surface of insect eyes (17). These structures were
76 found to generally be $\sim 150-250$ nm in height and spaced ~ 200 nm apart, which reduces
77 reflection across a broad range of wavelengths by creating a smoother gradient of
78 refractive indices between air and chitin (18). Nanostructure arrays have also been
79 identified on the wings of cicadas, which help to reduce surface reflection over the visible
80 spectrum (19).

81 Some lepidopterans possess modified wing scales that allow light to reach the
82 wing surface, which is composed of chitin and has some inherent transparency, but due to
83 the high refractive index of chitin, $n = 1.56$ (20), the wing surface reflects light. For
84 example, the butterfly *Methona confusa* (Nymphalidae: Ithomiini) has exposed wing
85 membrane that lacks nanostructures on the surface, and as a result, the wing is somewhat
86 transparent, but retains a high degree of reflectivity (Fig. 1A-C). Conversely, the longtail
87 glasswing, *Chorinea faunus* (Riodinidae), contains small, widely spaced scales and dome-
88 shaped chitin nanoprotuberances on the membrane that generate anti-reflective properties
89 (Fig. 1D-F) (21). The hawkmoth, *Cephonodes hylas* (Sphingidae), has nude wings due to
90 deciduous scales that fall out upon eclosion, and possesses anti-reflective nanostructures
91 on its wing surface that morphologically resemble insect corneal nipple arrays (9). Nipple
92 array nanostructures have also been characterized in transparent wing regions of the tiger
93 moth *Cacostatia ossa* (Erebidae) (22). Finally, the glasswing butterfly *Greta oto*
94 (Nymphalidae: Ithomiini) contains thin, vertically oriented scales, allowing the wing

95 surface to be exposed, along with nanopillars that coat the surface. These irregularly
96 arranged nanopillars feature a random height and width distribution and enable
97 omnidirectional anti-reflective properties (Fig. 1G-I) (10, 23). More recent studies have
98 explored aspects of structural diversity, optical properties, phylogenetic distribution, and
99 ecological relevance of transparency within a wide range of butterflies and moths,
100 highlighting that transparency has evolved multiple times independently and may present
101 evolutionary benefits (13, 24, 25).

102 Lepidoptera are proving to represent an excellent group to investigate
103 transparency on land, but the developmental processes underlying wing transparency are
104 currently unknown. This presents a gap in our understanding of lepidopteran wing
105 evolution and diversification, as transparent butterflies and moths contain multitudes of
106 intriguing scale modifications and sub-wavelength cuticular nanostructures (24, 25). We
107 therefore set out to explore the development of wing transparency in the glasswing
108 butterfly *Greta oto*, which belongs to a diverse tribe (~393 species) of predominantly
109 transparent neotropical butterflies (26). We applied confocal and transmission electron
110 microscopy to compare wing development, scale cytoskeletal organization, and
111 membrane surface nanostructures between clear and opaque wing regions. Using
112 chemical treatments, scanning electron microscopy, and gas chromatography–mass
113 spectrometry, we found that nanostructures on the wing membrane surface are made of
114 two layers: a lower layer of chitin-based nipple-like nanostructures, and an upper layer of
115 wax-based nanopillars composed predominantly of long-chain *n*-alkanes. Finally, by
116 removing the wax-based nanopillars, we demonstrate their role in dramatically reducing
117 reflection on the wing surface via optical spectroscopy and analytical simulations.

118

119 Results

120 Scale measurements in clear and opaque wing regions of adult *Greta oto*

121 We investigated features of scale density, scale morphology, and the amount of wing
122 surface exposed in wings of adult *Greta oto*. We focused on two adjacent regions within
123 the forewing for consistency: a clear region within the discal cell and an opaque region
124 that consists mainly of black scales near the M2-M3 crossvein. (Fig 1G,J). The clear wing
125 region contained two types of alternating scale morphologies: bristle-like scales and
126 narrow, forked scales, while within the opaque wing region, scale morphologies
127 resembled ‘typical’ butterfly pigmented scales: flat and ovoid with serrations at the tips
128 (Fig1. K,L). The mean density of scales (\pm SD) in the adult wing were significantly lower
129 within the clear region (107 ± 19 scales per mm^2) compared to the opaque region ($395 \pm$
130 23 scales per mm^2) (Student’s t-test, $P < 0.001$, $n = 3$ individuals, Fig. 1M). In the clear
131 region, forked scales were significantly smaller in size ($498 \pm 39 \mu\text{m}^2$) compared to the
132 bristle-like scales ($831 \pm 183 \mu\text{m}^2$), while in the opaque region, scales were the largest
133 ($3467 \pm 382 \mu\text{m}^2$) (ANOVA test, $n = 3$ individuals, Fig. 1N). Finally, the amount of
134 exposed wing membrane was significantly different between wing regions, with an
135 average of $83.1\% \pm 0.76$ and $2.4\% \pm 3.4$ exposed membrane in the clear and opaque
136 regions, respectively (Student’s t-test, $P < 0.001$, $n = 3$ individuals, Fig. 1O).

137

138 Morphogenesis and cytoskeletal organization of developing scale cells

139 To investigate developmental processes of wing and scale development, we performed
140 dissections of *G. oto* pupae at different time points (Fig. 2). As in other species of
141 Lepidoptera, the early pupal wing consisted of a thin bilayer of uniform epithelial tissue
142 and by 16 hours after pupal formation (APF) numerous epidermal cells had differentiated
143 to produce sensory organ precursor (SOP) cells, which could be identified by

144 fluorescently labelling tissue with DAPI (Fig. 2B,C) as the SOP's are larger than, and
145 positioned slightly basal to, the rest of the epidermal cells. The SOPs are precursors to the
146 scale and socket cells and are organized into parallel rows. At this early stage of wing
147 development, we observed that the clear wing region harbored a lower density of SOP
148 cells relative to the opaque wing region (Fig. 2B,C). We can therefore infer that early into
149 wing development, SOP cell patterning is differentially regulated between clear and
150 opaque regions, which impacts the adult wing scale density and the amount of wing
151 membrane surface exposed in different parts of the wing.

152 Next, we investigated cellular and cytoskeletal organization during scale growth
153 in clear and opaque wing regions, using simultaneous confocal imaging of fluorescently
154 labeled scale cell membrane (wheat germ agglutinin; WGA), and F-actin (phalloidin)
155 (Fig. 2D-I). We found that general aspects of scale development in *G. oto* follow those
156 previously reported in several butterfly and moth species by (6), with some notable
157 distinctions for modified scale growth in the clear wing regions of *G. oto*.

158 By 30 hours APF, the SOP cells have divided to produce the scale and socket cells
159 (Fig. 2D,E). The scale cell body lies internally within the wing, while the socket cell
160 associated with each scale cell lies in a more superficial position. At this pupal stage, the
161 morphological development of wing scale projections has begun, and the scale cells
162 develop as small buds containing short, densely packed parallel F-actin filaments.
163 Phalloidin staining showed the appearance of these small cylindrical buds containing F-
164 actin filaments, and WGA staining showed outlines of the membrane as the scale
165 outgrowths begin to project and elongate beyond the wing surface. At this stage, budding
166 scales in the clear wing region appeared morphologically similar to the unspecialized
167 opaque scales: roughly elongated balloon-shaped with numerous small actin rods fanning
168 out from the pedicel to the apical tip of the scale. In the clear region, early scale

169 projections showed alternating sizes. In the opaque region similar budding scales at a
170 higher density were found, with larger buds corresponding to future cover scales, and
171 smaller, shorter buds corresponding to future ground scales (Fig. 2D,E).

172 By 48 hours APF, scale cell extensions have grown and elongated (Fig. 2F,G).
173 The actin filaments have reorganized into smaller numbers of thick, regularly spaced
174 bundles along the proximal–distal axis of the scale just under the surface of the cell
175 membrane. At the base of the scales, fluorescent staining indicated that F-actin bundles
176 are tightly packed, while in more distal regions we could see an asymmetric distribution
177 of F-actin, with larger actin bundles in the adwing (facing the wing membrane) side of the
178 scales (movie S1). At this stage, scales in different regions of the wing had also started to
179 take on dramatically different morphologies. Scales in the clear region had elongated in a
180 vertical orientation and obtained two types of alternating morphologies: short and
181 triangular, or long and bristle-like outgrowths (Fig. 2F). The wings of other butterfly
182 species contain alternating ground and cover scales, in which the ground scales are
183 typically smaller in size than the cover scales, consistent with our observations of the
184 opaque regions of *G. oto* (Fig. 2F). Based on scale size and position, we interpret that
185 within the clear wing region of glasswing butterflies, the larger bristle-like scales are
186 modified cover scales and smaller forked scales are modified ground scales (Fig. 2F). In
187 the opaque region, scales have taken on a round and flattened morphology, similar to
188 what has been described in other colorful butterfly and moth species, with the ground
189 scales being shorter and wider than the cover scales (Fig. 2G).

190 By 60 hours APF, scale projections are even more elongated (Fig. 2H,I). The
191 triangular scales in the clear wing region have proceeded to generate two new branches,
192 which fork and elongate at the tips bidirectionally, while bristle-like scales have
193 elongated and curved (Fig. 2H). In the opaque region, scales were longer, wider, flatter,

194 and had developed serrations at the tips (Fig. 2I). F-actin bundles extended all the way to
195 the distal tips of these serrations, which is necessary to produce finger-like projections at
196 the tips of scales (6). Phalloidin staining also revealed that actin bundles were arranged in
197 more symmetrical patterns around the periphery of the bristle-like scale morphologies,
198 forked scales showed modified actin organization at the branching points, and actin
199 bundle asymmetry was greatest in developing flat opaque scales, with larger bundles
200 present on the adwing side (Fig. 2H,I).

201 **Ultrastructure analysis of developing bristle, forked and opaque scales**

202 To reveal ultrastructural detail of developing wing scale morphology, we performed
203 transmission electron microscopy (TEM) on pupal wing tissue of *G. oto* at 48 hours APF
204 (Fig. 3). In transverse sections, we could resolve distinct scale morphologies (bristle,
205 forked and opaque) and their associated cytoskeletal elements.

206 Bristle-like scales in the clear wing regions were circular in cross sections (Fig.
207 3A-C). We could also distinguish between distal and basal regions of bristle-like scales,
208 the latter of which had the presence of a surrounding socket cell in the cross section (Fig.
209 3B,C). TEM revealed that these bristle-like scales were ringed by peripheral bundles of
210 actin filaments, which lay spaced just under the cell membrane (Fig. 3B-C'). On the
211 adwing side of the scale, the actin bundles were larger and spaced closer to one another
212 relative to the abwing side, and in more distal regions of the bristle-like scale, the actin
213 bundles were more widely spaced and smaller in size. We also observed large populations
214 of microtubules (MTs) distributed throughout the developing scales, which were internal
215 relative to the actin bundles. Interestingly, we observed distinct patterns of microtubule
216 distribution within different developing scale morphologies. The cross section of bristle-
217 like scales revealed large populations of internal microtubules, which we identified due to
218 their characteristic ring shape and diameter of ~25 nm (Fig. 3B',C'). The circular ring

219 shape of microtubules in cross sections of both the basal and distal parts of the bristle-like
220 scale suggested that microtubules are all longitudinally oriented, running in the same
221 direction as the actin filaments, parallel to growth. We also observed that populations of
222 MTs are localized primarily away from the surface of the scale in its interior, and MTs
223 were fewer distally than basally (Fig. 3B',C').

224 In our TEM cross sections we also observed scale types that appeared more
225 triangular in shape, suggesting that these corresponded to developing forked scales within
226 the clear wing region (Fig. 3D,E). We observed that these scales were ringed by
227 peripheral bundles of crosslinked actin filaments, with thicker actin bundles on the
228 adwing side of the scale. Interestingly, we observed two internal bundles of actin
229 filaments that were not observed in bristle-like scale morphologies (Fig. 3E'). We also
230 note that there was variability in MT orientation, rather than the ubiquitous longitudinal
231 orientations observed in bristle-like scales.

232 Finally, developing opaque scales were easily identified in cross sections due to
233 their large size and flattened morphology (Fig. 3F,G). We observed peripheral bundles of
234 crosslinked actin filaments that were widely spaced and smaller in size in distal parts of
235 the scale (Fig. 3G-G'). We observed a clear asymmetry in actin bundle size, which were
236 thicker on the adwing side of the scale relative to the abwing surface. In opaque wing
237 regions, TEM micrographs revealed what appeared to be concentrated parallel-running
238 populations of MTs near the narrow base of the scales, and then a more mesh-like
239 network of MTs in more distal flattened regions, indicating that MTs have varying
240 orientations within different regions of the scale (Fig. 3G,G', fig. S1). In contrast to the
241 bristle-like scales, large, flattened opaque scales appeared to contain populations of MTs
242 that were more widely distributed and less dense.

243 In all scale types we observed the presence of numerous internal organelles and
244 vesicles, including mitochondria, electron dense vesicles and free ribosomes (Fig. 3, fig.
245 S1). We also observed that the actin bundles contained dense, hexagonally packed F-actin
246 filaments, supporting previous patterns for actin bundle formation in elongating insect
247 scales (fig. S1). The neck regions of different scale morphologies were predominantly
248 filled with longitudinally oriented microtubules, actin bundles, and mitochondria.
249 Longitudinal views also supported that MTs are numerous in the outgrowing scale, and
250 their spatial arrangement differed with scale position and shape. More mature scales
251 around 120 hours APF exhibited developed ridge morphologies and thickened cuticle
252 layers (fig. S1).

253 **Ontogeny of wing membrane nanostructures**

254 The clear wing regions of *G. oto* contain nanopillars that cover the surface of the
255 membrane (Fig 1I, Fig 4A). These nanopillars were previously characterized in adult
256 wings, which feature an irregular height distribution and help to generate omnidirectional
257 anti-reflective properties (10). To gain insight into the development of these
258 nanostructures, we examined the surface of the wing membrane epithelial cells with TEM
259 (Fig. 4B-F). At 60 hours APF, a perpendicular section through the wing epithelia
260 showed a continuous epithelial lamina (Fig. 4B,C). We observed the epithelial cells
261 contained microvilli (MV), which appeared as slender linear extensions from the inner
262 margins of the developing cells that insert into electron-dense material (Fig. 4B,C). The
263 surface layer of the epithelia appeared as an extracellular lamellar system, and lamina
264 evaginations appeared in the section as domes distal to the microvillar extensions (Fig.
265 4C). By 72 hours APF, we observed a thin outer layer of the epicuticle that rose above
266 the epidermal cells and by 120 hours APF, we found that this upper layer above the
267 microvilli contained what appear to be dome-shaped protrusions and thickened cuticle,

268 possibly secreted from regularly spaced microvilli (Fig. 4D,E). Finally, in our TEM
269 cross section of a fully developed adult wing of *G. oto*, we observed that the membrane
270 surface harbors dome-shaped nanoprotusions with similar morphologies to insect
271 corneal surface nipple arrays (e.g. 9, 17), which we refer to throughout the text now as
272 “nipple nanostructures”, and an upper layer containing pillar-like protrusions, which we
273 refer to as “nanopillars”, that featured a more irregular height distribution (Fig. 4F).
274 These results show early subcellular processes of developing nanopillars within the
275 clear wing region, which arise distal to microvillar extension in epithelial cells.

276 **Topographical organization and biochemical composition of wing surface** 277 **nanostructures**

278 Based on our EM results of membrane nanostructures, we investigated the topographical
279 organization and biochemical composition of the adult wing surface. To do so, we treated
280 individual, disarticulated adult *G. oto* wings in two ways: by 1) physically removing wing
281 surface nanostructures by gently pressing and rubbing a wing in between paper and
282 Styrofoam (after 9) and 2) testing the wing surface structures for solubility in organic
283 solvents, including hexane and chloroform to extract lipids (after 27). We then performed
284 SEM to compare wing surface topography of untreated and treated wing samples (Fig.
285 5A-C'). SEM confirmed that the first treatment partially or completely removed
286 nanostructures across the wing membrane surface (Fig. 5B). In a region of partial
287 removal, we could identify smaller, dome-shaped nipple nanostructures underneath the
288 top layer of nanopillars (Fig. 5B'). SEM of the chemically treated wing surface revealed
289 that the upper layer of irregularly sized nanopillars were completely removed, revealing a
290 layer of regularly arranged dome-shaped nipple nanostructures that did not dissolve
291 through chloroform or hexane exposure (Fig. 5C,C'). Therefore, we hypothesized that the

292 upper layer of irregularly sized nanopillars consisted of a secreted wax-based material,
293 which sits above smaller chitin-based nipple nanostructures.

294 To test this hypothesis, we extracted the surface layer of *G. oto* clear wing regions
295 with either hexane or chloroform and analyzed the chemical composition by gas
296 chromatography–mass spectrometry (GC-MS). We found that the chemical profile
297 generated by both hexane and chloroform extracts yielded similar results (Fig. 5D). In all
298 extracts, we identified two straight-chain alkanes that made up approximately 2/3 of the
299 compounds detected: $41.64 \pm 5.75\%$ pentacosane ($C_{25}H_{52}$) and $23.32 \pm 5.35\%$
300 heptacosane ($C_{27}H_{56}$) (Table S1). The remaining compounds were primarily composed of
301 slightly larger methyl-branched alkanes (monomethyl and dimethyl C27, C29 and C31)
302 and esters. Therefore, our results suggest that in *G. oto* there are two components to wing
303 surface ultrastructure: procuticle-based nipple nanostructures, and an upper epicuticular
304 layer of irregularly sized nanopillars, composed mainly of straight chain alkanes (Fig.
305 5D,E).

306 **Anti-reflective properties of wax-based nanopillars**

307 To address whether the wax-based nanopillars play a role in wing reflection, we measured
308 the reflectance spectra of untreated and hexane-treated wings (Fig. 6). Additionally, we
309 measured nanostructure geometries and membrane thickness from wing SEM cross
310 sections ($n = 6$), and determined the average distance between two nanostructures as $d =$
311 174 nm, conical shaped cuticular nipple nanostructures height, $h_p = 77$ nm, wax-based
312 irregular nanopillars radius, $r_{np} = 53$ nm, mean height, $h_{np} = 224$ nm and variance $\sigma_{np} =$
313 49.3 nm, and membrane thickness, $h_m = 746$ nm and variance $\sigma_m = 43$ nm (Fig. 6B,D, fig.
314 S2). On the basis of SEM micrographs for treated and untreated samples, we modeled
315 three wing architectures consisting of 1) nanopillars with variable height together with
316 cuticle-based nipple nanostructures on the wing membrane, 2) cuticle-based nipple

317 nanostructures on wing membrane and 3) wing membrane without any nanostructures, to
318 simulate the optical properties for different conditions (Fig. 6E). The simulated
319 reflectance data of the untreated and treated conditions in Fig. 6F closely resembled the
320 experimental ones. In untreated wings of *G. oto*, we found that transparent regions have a
321 low total diffuse reflection of about 2%, which is in line with previous reflectance
322 measurements of this species (Fig. 6F, 10). By contrast, the hexane treated wings without
323 the upper layer of wax nanopillars had about 2.5 times greater reflectance relative to the
324 untreated wings, and generated an iridescent thin film spectra, even though they harbored
325 dome-shaped nipple nanostructures (Fig. 6D,F).

326 For simulated data, the overall reflectance ratio of the hexane treated wing to that
327 of the untreated was approximately three, similar to experimental reflectance data (Fig.
328 6F, Table S2). Most importantly, the simulated results for the untreated wing with wax-
329 based irregular nanopillars make reflectance more uniform across wavelengths, which
330 reduces the iridescent effect of the wing membrane. Finally, we simulated a thin film
331 membrane without any nanostructures, which showed reflectance (averaged from all
332 wavelengths) of the membrane itself to be $8.81 \pm 3.46\%$, whereas the treated and
333 untreated wing reflections were $5.78 \pm 2.82\%$ and $1.93 \pm 0.77\%$, respectively (Fig. 6F).
334 While treated wings harboring dome-shaped nipple nanostructures reduced the overall
335 reflectance relative to the membrane only, their effect was not strong enough to reduce
336 reflectance spectra oscillation. The wax-based irregular nanopillars on top introduced a
337 more gradual transition between refractive indices to lessen the oscillation by
338 approximately five-fold, in addition to reducing overall reflection (Fig, 6F). Additionally,
339 we simulated the three wing architecture models considering different mean membrane
340 thicknesses and variance in membrane thickness (fig. S3). We found that variance in wing
341 membrane thickness reduced reflectance spectra oscillations, rather than mean membrane

342 thickness alone, and more peaks appear in the visible spectrum with increasing thickness
343 of the membrane. (fig. S3, Table S3). Overall, these results demonstrate that the non-
344 constant architecture of the wing membrane and wax-based irregular nanopillars on the
345 wing surface of *G. oto* function to dramatically enhance anti-reflective properties.

346 Discussion

347 Butterflies and moths have evolved sub-wavelength anti-reflective structural innovations
348 on their wings that enable them to be transparent. Here we report the details of pupal
349 wing development and cytoskeletal organization in the glasswing butterfly, *Greta oto*, as
350 well as insights into the ontogeny and biochemical basis of wing surface nanostructures
351 that reduce reflection.

352 The arrangement of unicellular projections in insect integument, such as bristles
353 and scales, has been a model for research on cellular pattern formation (28). Shortly after
354 pupation, sensory organ precursor (SOP) cells develop from a monolayer of epithelial
355 cells into orderly arrangements, then differentiate into scale and socket cells. In the
356 present study, we found that early SOP cell patterning impacts the final adult scale
357 density in *G. oto* and this feature of spacing scale cells farther apart, and therefore
358 reducing the overall density of scales, is an initial step to generate clear wings. During
359 early pupal development, the receptor molecule Notch is expressed in a grid-like pattern
360 in the wing epithelium (29). This may contribute to the parallel rows of uniformly spaced
361 SOP cells that express low levels of Notch, likely through a lateral inhibition mechanism.
362 The low-Notch SOP cells express a homolog of the *achaete-scute* proneural transcription
363 factors, which likely plays a role in scale precursor cell differentiation (30). Notch-
364 mediated lateral inhibition could establish a dense population of ordered SOP cells in the
365 developing wing, resulting in a characteristic ratio of scale-building and epithelial cells.

366 Future studies should investigate if modifications in Notch signaling play a role in scale
367 cell patterning in clearwing butterflies and moths, many of which contain reduced
368 densities of scale cells (24, 25).

369 The range of morphological diversity among scales and bristles within
370 Lepidoptera likely results developmentally from components or modifiers of the
371 cytoskeletal structures and cell membrane. One study surveyed a wide range of
372 developing butterfly and moth scales and identified that F-actin is required for several
373 aspects of scale development, including scale cell elongation and proper orientation (6).
374 In the present study, we found that *G. oto* serves as an excellent model to study
375 differences in bristle and scale morphogenesis, as the wing contains a wide range of
376 different scale types. In the developing bristle-like scales, we find symmetrical actin
377 bundles that outline the cell periphery and a large population of longitudinally running
378 interior microtubules. This is similar to what has been described for developing bristles in
379 *Drosophila melanogaster* pupae, which contain peripheral bundles of cross-linked actin
380 filaments and a large population of microtubules that run longitudinally along the bristle
381 (31). Recently, (32) showed that actin bundles play different roles in shaping scales and
382 bristles in the mosquito *Aedes aegypti*, in which developing bristles contained
383 symmetrically organized actin bundles, while actin bundle distribution in scales became
384 more asymmetrically organized. Given that actin dynamics play a variety of roles in
385 regulating the development of bristles and scales (6, 7, 32, 33), we hypothesize that
386 modifications in F-actin organization of scales in the transparent wing of *G. oto* are
387 responsible in part for their narrow bristle-like and forked morphologies. In *D.*
388 *melanogaster*, subunits of actin are rapidly added to the barbed ends of the actin filaments
389 of bristles, relying on actin polymerization and bundling for this purpose, and cross-
390 linking proteins are required early to bring filaments together (31). One cross-linking

391 protein, Fascin, connects filaments together into hexagonally packed bundles. Our TEM
392 of actin bundles, along with previous studies, support a similar mechanism of hexagonally
393 packed F-actin bundles in Lepidoptera (Fig. 3, fig. S1) (6, 7).

394 In animal cells, microtubules have been frequently observed in arrangements
395 parallel to the long axis of cellular extensions, such as axons, dendrites, and developing
396 lepidopteran scales (33). In an analysis of moth scale development, major shape changes
397 were found to be correlated with changes to the orientation of the cytoplasmic
398 microtubules (33). In the present study, we identified large populations of microtubules
399 organized throughout developing scales and showed that microtubules are more
400 concentrated at the base of the scale. We also found that microtubules exhibit different
401 distributions and orientations relative to distinct scale morphologies, namely between
402 bristle, forked, and flat, round scales. In *D. melanogaster*, it has been suggested that
403 bristle microtubules play a role in elongation, noting that they are highly stable, form at
404 the start of the elongation, and then extend along the shaft as the cell elongates (30). A
405 more recent reinvestigation of the role of MTs in *D. melanogaster* bristle elongation
406 suggests that two populations of microtubules help to guide bristle development: dynamic
407 microtubules (with mixed polarity) add bulk to the bristle cytoplasm and are thought to
408 contribute proper axial growth, while stable microtubules act to polarize the axis of bristle
409 elongation and are believed to aid organelle and protein distribution (34, 35). It would be
410 interesting for future studies to functionally characterize the role microtubules play in the
411 development of lepidopteran scales. Overall, we found conservation of developmental
412 processes in scale formation relative to other previously described Lepidoptera, with
413 notable differences in clear versus opaque wing regions. These findings lend further
414 support that general patterns of scale development, including patterns of F-actin
415 localization and microtubule distribution, seem to be well conserved in Lepidoptera, and

416 that modifications of scale morphology to achieve clearwing phenotypes, such as narrow
417 bristle-like and forked scales, likely involve alteration of cytoskeletal organization during
418 scale growth.

419 Chitinous wing membrane has a higher refractive index than air, so as a
420 mechanism that reduces glare, some clearwing species have evolved sub-wavelength anti-
421 reflective nanostructures (9, 10). In this study, we identified the early developmental
422 processes of nanostructures that arise in the wing epithelium. We also note interesting
423 parallels of our observations to previous descriptions of developing nanostructures on the
424 surface of insect cornea. Early data on pupal development of corneal nanostructures
425 were produced by detailed electron microscopy studies, showing that corneal nipples
426 emerge during lens formation, and a chitinous layer may be subsequently secreted
427 underlying the nanostructure (36). In these observations, development of initial laminar
428 patches formed on top of underlying microvilli. Subsequently, nanostructures (termed
429 nipple structure array) formed on the surface, with the tips of microvilli still attached to
430 the inner surface. Another study subsequently investigated pupal eye development in *D.*
431 *melanogaster* and identified features of corneal nipple array formation that matched
432 observations previously made in moth eye nanostructure development (37). Gemne (36)
433 proposed that the corneal nanostructures originate from secretion by the regularly spaced
434 microvilli of the cone lens cells, although there is still debate about the exact nature of
435 how microvilli pre-pattern nanostructure arrays (38). Our TEM results provide insight
436 into the early developmental processes of anti-reflective nanostructure formation in the
437 wings of *G. oto*, highlighting certain similarities to nipple array development in insect
438 cornea. It would be interesting for future work to explore if features of nanostructure
439 formation arose independently in insect cuticle as a mechanism to reduce surface
440 reflection.

441 In contrast to previously described highly ordered nipple arrays on insect eyes
442 (e.g. 18, 38), the irregularly sized anti-reflective nanopillars in the clear regions of *G. oto*
443 wings consist of an upper layer of wax-based epicuticle sitting above procuticle-based
444 nipple nanostructures. Insect cuticle is an extracellular matrix formed by the epidermis
445 and composed of three layers: the outermost envelope, the middle epicuticle and the inner
446 procuticle (39). The envelope and the epicuticle are composed mainly of lipids and
447 proteins, while the procuticle contains the polysaccharide chitin. Many terrestrial
448 arthropods deposit a layer of wax lipids on the surface of their cuticle, which reduces
449 evaporative water loss (40). In some species of dragonfly, epicuticular wax-based
450 nanostructures have also been demonstrated to play a role in generating optical properties,
451 such as an ultraviolet reflection (27). In mature males of the dragonflies, a dense wax
452 secretion composed of long-chain methyl ketones, in particular 2-pentacosanone, was
453 found to contribute to the UV reflection properties. The chemical composition of
454 nanopillars on the wing surface of cicadas, which have been shown to contribute to
455 wettability and antimicrobial properties, and found that the major epicuticular
456 components are fatty acids and hydrocarbons ranging from C_{17} to C_{44} (41). Another study
457 exploring the molecular organization of dragonfly wing epicuticle found that the major
458 components identified were fatty acids and *n*-alkanes with even numbered carbon chains
459 ranging from C_{14} to C_{30} (42). Here, we identified that the epicuticular layer of irregularly
460 sized anti-reflective nanopillars in *G. oto* appear to be composed mainly of *n*-alkanes,
461 including pentacosane (C_{25}) and heptacosane (C_{27}) and showed the importance of these
462 structures to attain better transparency.

463 Due to thin film optics, the thin membranes of insect wings sometimes reflect
464 distinct structural coloration and iridescence (43). However, variability and non-constant
465 thickness render the wing membranes as non-ideal thin films, and additional surface

466 nanoprotusions can introduce a gradient of refractive indices that reduces thin film
467 reflections (44). For instance, membrane thickness was found to vary over the transparent
468 wings of the damselfly *Hetaerina americana* from below 1 μm to up to 3 μm , yet
469 membrane nanoprotusions acted as an effective impedance matching device to reduce
470 reflectance (44). In that study, average reflectance spectra for the Andromica clearwing
471 butterfly *Greta andromica* was also calculated, although the wing was treated as a thin
472 film, and did not address membrane surface nanostructures. By varying thickness in a
473 Gaussian way while maintaining average thickness, (44) found that an increasing width of
474 the Gaussian progressively reduced modulation of the reflectance spectrum. Similarly, in
475 the present study, measurements from SEM cross sections of *G. oto* transparent wings
476 indicate that the membrane thickness is non-constant, and in our optical simulations,
477 variance in membrane thickness was found to be an important parameter for reduced
478 reflectance spectra modulation (fig. S3). Overall, we found that variance in membrane
479 thickness and wax-based nanostructures with irregular height distributions in *G. oto*
480 reduce iridescence and maintain anti-reflection properties, which likely aid in crypsis
481 (11).

482 Turing reaction-diffusion mechanisms have been proposed as a model for the
483 formation of various corneal nanostructure morphologies (such as spacing, height, and
484 spatial organization) during insect eye development (reviewed in 38). Although the
485 degree of height irregularity of nanopillars is important for achieving omnidirectional
486 anti-reflection in *G. oto*, we do not yet understand how the wax nanopillars are generated
487 to vary in height. Perhaps the pressure of the wax secretion varies across the microvillar
488 extensions' area, similar to how nozzle area plays a role in the propulsion force, and tunes
489 the height of the nanopillars in the process. In such a scenario, the degree of the height
490 variation could be synthetically engineered depending on the two-dimensional

491 nanopatterned mask design in the biomimetic processes, like molding or imprinting
492 techniques. Additionally, others have generated three-dimensional wax structures by
493 using *n*-alkanes, noting that wax-based crystals can generate different shapes, sizes and
494 densities depending on the chain length (45). Future work should investigate the possible
495 role of alkanes, and the two-dimensional surface growth geometry, in generating three-
496 dimensional anti-reflective nanostructures and potential applications for biomimetics. Our
497 exploration of *Greta oto* wing development can serve as a model for understanding how
498 transparent phenotypes evolved within Ithomiini, a diverse tribe of neotropical butterflies
499 that act as mimicry models for numerous species of Lepidoptera (26), as well as more
500 distantly related butterfly and moth species.

502 **Materials and Methods**

503 **Samples**

504 Glasswing butterfly (*Greta oto*) pre-pupae were purchased from Magic Wings Butterfly
505 House (Deerfield, Massachusetts, USA) and reared on *Cestrum nocturnum* (Solanaceae)
506 leaves at 27°C and 60% humidity on a 16:8 hour light:dark cycle at the Marine Biological
507 Laboratory (Woods Hole, MA) under the United States Department of Agriculture permit
508 number P526P-19-02269. At the appropriate time of development, pupal wings were
509 dissected and age was recorded as hours after pupal case formation (h APF) as in (6). The
510 average timeline from pupation to eclosion (adult emergence) for *G. oto* at 27°C is about
511 7 days, and we report our time series here which covers early aspects of wing scale
512 development.

514 **Optical imaging and scale measurements**

515 Images of whole mounted specimens were taken with a Canon EOS 70D digital camera
516 with an EF 100mm f/2.8L macro lens. High-magnification images of disarticulated wings
517 were taken with a Keyence VHX-5000 digital microscope. Scale density was determined
518 by counting the numbers of scales in a 1 mm² area. Scales were also removed from the
519 wings, laid flat onto a slide, and Keyence software was used to measure the surface area
520 of individual scales. Images of clear and opaque regions were processed with Keyence
521 software to measure the percentage of area covered by scales. Sample size was equal to
522 three individual butterflies reared in the same cohort, in which four measurements for
523 each individual were averaged. We performed Student's t-tests for scale density and
524 percent of exposed membrane, and one-way ANOVA test for scale surface area
525 comparisons.

526 **Confocal microscopy**

527 For confocal microscopy of fixed tissue, pupal wings were dissected and fixed in PIPES,
528 EGTA, MgSO₄ (PEM) buffer with 3.7% paraformaldehyde for 20-30 minutes at room
529 temperature, as described previously (6). Fixed wings were incubated in 1X PBS+0.1%
530 Triton-X 100 (PT) with 1:200 dilution of phalloidin, Alexa 555 conjugated (Invitrogen
531 A34055), and Wheat Germ Agglutinin, Alexa 647 conjugated (Invitrogen W32466) at a
532 dilution of 1:200 overnight at 4°C. Wings were washed in PT and then placed in 50%
533 glycerol:PBS with 1 µg/mL DAPI overnight at 4°C. Wing samples were placed on
534 microscope slides and mounted in 70% glycerol:PBS. A coverslip (#1.5 thickness) was
535 applied, and each preparation was sealed with nail polish. Slides of fixed tissue were
536 examined with an LSM 880 confocal microscope (Carl Zeiss, Germany) with 40x and
537

538 63x objectives. Confocal images and movies were generated using Imaris Image Analysis
539 Software (Bitplane, Oxford Instruments, UK).

541 **Scanning electron microscopy**

542 We cut 2mm square pieces from dry wings, coated them with a 10 nm layer of gold using
543 the BIO-RAD E5400 Sputter Coater, and imaged with a Hitachi TM-1000 SEM at 5 kV.
544 Top-view and cross section SEM images were analysed with ImageJ 1.52 to measure
545 membrane thickness and nanostructure dimensions (n = 6).

547 **Transmission electron microscopy**

548 For transmission electron microscopy, wings of *Greta oto* pupae were dissected and fixed
549 in 2% glutaraldehyde, 2% paraformaldehyde in 0.1 M sodium cacodylate buffer overnight
550 at 4°C (pH 7.4). Samples were then rinsed in 0.1 M cacodylate buffer (pH 7.4) and post-
551 fixed in 1% aqueous osmium tetroxide in 0.1M cacodylic buffer overnight at 4°C, then
552 rinsed in water. Samples were en bloc stained with 1% uranyl acetate in water and then
553 rinsed in water. Samples were dehydrated through a graded ethanol series (50–100% in
554 10% steps), rinsed in propylene oxide, then infiltrated in 50% resin and propylene oxide
555 overnight. Samples were infiltrated with Epon/Alardite embedding medium (70%, 80%,
556 95% to 100% steps) and polymerized at 60°C for two days. Thin sections (~70nm) were
557 cut on an Ultramicrotome RMC PowerTome XL using a Diatome diamond knife. Digital
558 images were taken using a JEOL 200 transmission electron microscope (Jeol, USA).

560 **Wing surface wax extraction and analysis**

561 To identify the molecular composition of the transparent wing surface, we pooled wing
562 dissections from three individual adults and performed two replicates for chloroform-

563 based extractions and two replicates for hexane-based extractions (after 26). First, the
564 samples were soaked with 100 μ L of either hexane or chloroform and gently mixed for 15
565 minutes on a Thermolyne RotoMix 51300. The liquid solutions containing dissolved wing
566 surface compounds were then transferred to glass vials with fixed microvolume inserts
567 and the solvent was evaporated under a stream of high-purity nitrogen gas (99.99%).
568 Dried extracts were re-dissolved in fixed volumes of hexane (10 μ L), and half of the
569 extract (5 μ l) was injected by automatic liquid sampler into a gas chromatograph coupled
570 with a mass selective detector (GC: 7890A; MS: 5975C; Agilent Technologies, USA)
571 operating in electron impact mode. The injection was performed in a split/splitless
572 injector in the splitless mode. Separation of compounds was performed on a fused silica
573 capillary column (DB-5MS, 30 m \times 0.32 mm \times 0.25 μ m, Agilent J&W GC columns,
574 USA) with a temperature program starting from 80°C for 5 min and increasing by 80°C
575 per min to 200 °C, followed by an increase of 5 °C per min to 325 °C which was held for
576 3 min, with helium used as the carrier gas, positive electron ionization (70 eV), Analog to
577 Digital (A/D) sampling rate was set at 4, and the scan range was m/z 40.0 to 650.0.
578 Chemical data processing was carried out using the software “Enhanced Chemstation”
579 (Agilent Technologies, USA). We retained peaks with abundances greater than 0.25% of
580 the total and compounds were identified according to their retention indices, diagnostic
581 ions, and mass spectra, which are provided in Table S1. For some peaks, it was not
582 possible to narrow the identity to a single specific compound because (1) some low
583 abundance substances produced poor quality mass spectra, (2) multiple compounds could
584 have produced the observed fragmentation patterns and/or (3) multiple compounds may
585 have co-eluted at the same retention time.
586

Optical measurements

The wing reflection measurements were performed on a Cary 5000 UV-Vis-NIR spectrophotometer, equipped with a light source of tungsten halogen and an integrating sphere diffuse reflectance accessory (Internal DRA 1800). Wing measurements from the dorsal wing surface ($n = 6$) were recorded with unpolarized light with a spot size of 100 μm for an incident angle of 8° to avoid the loss of direct specular reflectance component through the aperture. All measurements were taken in the dark to avoid possible stray illumination from the surrounding environment. A reference measurement was done with a calibrated commercial white spectralon standard to calculate the relative diffuse reflectance. The reflectance measurements and mean data are presented in Table S2.

Optical simulations

The reflectance of the wing membrane before and after chemical treatment by hexane was analytically modeled using effective medium theory and transfer matrix method (10, 18). First, the effective volume fraction of the nanoprotuberances before and after the chemical treatment were based on measurements taken from SEM micrographs of the wings. We used the average distance between two hexagonally arranged nanostructures, d , conical shaped nipple nanostructures with height, h_p , wax-based irregular nanopillars with radius, r_{np} , mean height, h_{np} and variance σ_{np} , and membrane thickness, h_m and variance σ_m (fig. S2). We considered a Gaussian distribution of irregular nanopillar height, as described previously (10). We also modeled the membrane thickness with Gaussian distribution to replicate the experimental membrane modulation in the calculation (44, 46). The total volume fraction of the untreated wing along the height h can be given by:

$$\frac{\pi r_{np}^2}{\sqrt{3}d^2} \operatorname{erfc}\left(\frac{h-h_{np}}{\sigma_{np}\sqrt{2}}\right);$$

zone: dorsal wax based nanopillar

$$\frac{\pi}{\sqrt{3}d^2} \left(r_{np} + \left(\frac{d}{2} - r_{np}\right) \left(1 - \frac{h}{h_p}\right) \right)^2;$$

zone: dorsal chitin-based nipple array

$$f_{untreated}(h) = 1;$$

zone: chitin membrane

$$\frac{\pi}{\sqrt{3}d^2} \left(r_{np} + \left(\frac{d}{2} - r_{np}\right) \left(1 - \frac{h}{h_p}\right) \right)^2;$$

zone: ventral chitin-based nipple array

$$\frac{\pi r_{np}^2}{\sqrt{3}d^2} \operatorname{erfc}\left(\frac{h-h_{np}}{\sigma_{np}\sqrt{2}}\right);$$

zone: ventral wax based nanopillar

611 where, $\operatorname{erfc}(x) = \frac{2}{\sqrt{\pi}} \int_x^\infty e^{-t^2} dt$ is the complementary error function.

612 The volume fraction of the treated wing without the irregular nanopillars will be:

$$\frac{\pi}{2\sqrt{3}} \left(1 - \frac{h}{h_p}\right);$$

zone: dorsal chitin-based nipple array

$$f_{treated}(h) = 1;$$

zone: chitin membrane

$$\frac{\pi}{2\sqrt{3}} \left(1 - \frac{h}{h_p}\right);$$

zone: ventral chitin-based nipple array

613 After determining the volume fraction, the corresponding refractive index changes along
 614 the wing at any height h was calculated using the effective medium theory with the
 615 Maxwell-Garnett approximation as shown in Fig. 6E, fig. S2. The refractive indices of the
 616 different materials were considered as $n_{\text{air}} = 1$, $n_{\text{chitin}} = 1.56 + i0.008$ (20, 21) and we
 617 considered $n_{\text{wax}} = 1.39$ (based on 47). Afterwards, the transfer matrix method computed
 618 the reflectance from the stratified medium with calculated refractive index profiles as
 619 shown in Fig. 6E for the unpolarized condition (taking the average of both s- and p-
 620 polarization) at an incident angle of 8° . The membrane-only reflection at normal incident
 621 light can be directly calculated from (46):

$$R(\lambda) = \int_0^\infty \left| \frac{r(1 - e^{-2i\delta})}{1 - r^2 e^{-2i\delta}} \right|^2 \frac{1}{\sigma_m \sqrt{2\pi}} e^{-\frac{(h-h_m)^2}{2\sigma_m^2}} dh.$$

622

623 Where, $\delta = (2\pi n_{\text{chitin}}h)/\lambda$ is the phase delay introduced by the membrane thickness of h ,
624 and r is the reflection coefficient at the air-chitin boundary governed by Fresnel's
625 equation for a normal incident light, i.e., $r = (1 - n_{\text{chitin}}) / (1 + n_{\text{chitin}})$.

626 **References and Notes**

- 627 1. P. Beldade, P. M. Brakefield. The genetics and evo–devo of butterfly wing patterns.
628 *Nature Reviews Genetics*. **3**, 442-52 (2002).
- 629 2. R. O. Prum, T. Quinn, R. H. Torres. Anatomically diverse butterfly scales all produce
630 structural colours by coherent scattering. *Journal of Experimental Biology*. **209**, 748-
631 65. (2006).
- 632 3. L. E. Gilbert, M. C. Singer. Butterfly ecology. *Ann. Rev. Ecol. Syst.* **6**, 365-95 (1975).
- 633 4. D. G. Stavenga, H. L. Leertouwer, B. D. Wilts. Coloration principles of nymphaline
634 butterflies–thin films, melanin, ommochromes and wing scale stacking. *J. Exper. Biol.*
635 **217**, 2171-80 (2014).
- 636 5. R. C. Thayer, F. I. Allen, N. H. Patel. Structural color in *Junonia* butterflies evolves
637 by tuning scale lamina thickness. *Elife*. **9**, e52187 (2020).
- 638 6. A. Dinwiddie, R. Null, M. Pizzano, L. Chuong, A. L. Krup, H. E. Tan, N. H. Patel.
639 Dynamics of F-actin prefigure the structure of butterfly wing scales. *Develop. biol.*
640 **392**, 404-18 (2014).
- 641 7. A. R. Day, J. J. Hanly, A. Ren, A. Martin. Sub-micrometer insights into the
642 cytoskeletal dynamics and ultrastructural diversity of butterfly wing scales.
643 *Developmental Dynamics*. **248**, 657-70 (2019).
- 644 8. P. P. Goodwyn, Y. Maezono, N. Hosoda, K. Fujisaki. Waterproof and translucent
645 wings at the same time: problems and solutions in butterflies. *Naturwissenschaften*.
646 **96**, 781-7 (2009).
- 647 9. A. Yoshida, M. Motoyama, A. Kosaku, K. Miyamoto. Antireflective
648 nanoprotuberance array in the transparent wing of a hawkmoth, *Cephonodes hylas*.
649 *Zoological sci.* **14**, 737-41 (1997).
- 650 10. R. H. Siddique, G. Gomard, H. Hölscher. The role of random nanostructures for the
651 omnidirectional anti-reflection properties of the glasswing butterfly. *Nature*
652 *communications*. **6**, 1-8 (2015).
- 653 11. M. Arias, J. Mappes, C. Desbois, S. Gordon, M. McClure, M. Elias, O. Nokelainen,
654 D. Gomez. Transparency reduces predator detection in mimetic clearwing butterflies.
655 *Func. Ecol.* **33**, 1110-9 (2019).
- 656 12. M. Arias, M. Elias, C. Andraud, S. Berthier, D. Gomez. Transparency improves
657 concealment in cryptically coloured moths. *J. Evol. Biol.* **33**, 247-52 (2020).

- 658 13. M. McClure, C. Clerc, C. Desbois, A. Meichanetzoglou, M. Cau, L. Bastin-Héline, J.
659 Bacigalupo, C. Houssin, C. Pinna, B. Nay, V. Llaurens. Why has transparency
660 evolved in aposematic butterflies? Insights from the largest radiation of aposematic
661 butterflies, the Ithomiini. *Proc. Royal Soc. B.* **286**, 20182769 (2019).
- 662 14. S. Johnsen. Hidden in plain sight: the ecology and physiology of organismal
663 transparency. *The Biological Bulletin.* **201**, 301-18 (2001).
- 664 15. S. Johnsen. Hide and seek in the open sea: pelagic camouflage and visual
665 countermeasures. *Annual review of marine science.* **6**, 369-92 (2014).
- 666 16. L. E. Bagge. Not as clear as it may appear: challenges associated with transparent
667 camouflage in the ocean. *Integ. compar. biol.* **59**, 1653-63 (2019).
- 668 17. C. G. Bernhard, W. H. Miller. A corneal nipple pattern in insect compound eyes. *Acta*
669 *Physiologica Scandinavica.* **56**, 385-6 (1962).
- 670 18. D. G. Stavenga, S. Foletti, G. Palasantzas, K. Arikawa. Light on the moth-eye corneal
671 nipple array of butterflies. *Proc. Royal Soc. B: Biological Sciences.* **273**, 661-7
672 (2006).
- 673 19. Y. F. Huang, Y. J. Jen, L. C. Chen, K. H. Chen, S. Chattopadhyay. Design for
674 approaching cicada-wing reflectance in low-and high-index biomimetic
675 nanostructures. *ACS nano.* **9**, 301-11 (2015).
- 676 20. P. Vukusic, J. R. Sambles, C. R. Lawrence, R. J. Wootton. Quantified interference
677 and diffraction in single Morpho butterfly scales. *Proc. Royal Soc. London. Series B:*
678 *Biol. Sci.* **266**, 1403-11 (1999).
- 679 21. V. Narasimhan, R. H. Siddique, J. O. Lee, S. Kumar, B. Ndjamen, J. Du, N. Hong, D.
680 Sretavan, H. Choo. Multifunctional biophotonic nanostructures inspired by the
681 longtail glasswing butterfly for medical devices. *Nature nanotechnology.* **13**, 512-9
682 (2018).
- 683 22. O. Deparis, S. R. Mouchet, L. Dellieu, J. F. Colomer, M. Sarrazin. Nanostructured
684 surfaces: bioinspiration for transparency, coloration and wettability. *Mater. Today*
685 *Proc. S.* **1**, 122-9 (2014).
- 686 23. V. R. Binetti, J. D. Schiffman, O. D. Leaffer, J. E. Spanier, C. L. Schauer. The natural
687 transparency and piezoelectric response of the *Greta oto* butterfly wing. *Integr. Biol.*
688 **1**, 324-9 (2009).
- 689 24. D. Gomez, C. Pinna, J. Pairraire, M. Arias, J. Barbut, A. Pomerantz, C. Nous, W. D.
690 de Marcillac, S. Berthier, N. Patel, C. Andraud, M. Elias. Transparency in butterflies

- 691 and moths: structural diversity, optical properties and ecological relevance. *bioRxiv*.
692 doi: <https://doi.org/10.1101/2020.05.14.093450> (2020).
- 693 25. C. Pinna, M. Vilbert, S. Borenztajn, W. D. de Marcillac, F. Piron-Prunier, A.
694 Pomerantz, N. Patel, S. Berthier, C. Andraud, D. Gomez, M. Elias. Convergence in
695 light transmission properties of transparent wing areas in clearwing mimetic
696 butterflies *bioRxiv*. doi: <https://doi.org/10.1101/2020.06.30.180612> (2020).
- 697 26. M. Elias, Z. Gompert, C. Jiggins, K. Willmott. Mutualistic interactions drive
698 ecological niche convergence in a diverse butterfly community. *PLoS biology*. **6**, e300
699 (2008).
- 700 27. R. Futahashi, Y. Yamahama, M. Kawaguchi, N. Mori, D. Ishii, G. Okude, Y. Hirai, R.
701 Kawahara-Miki, K. Yoshitake, S. Yajima, T. Hariyama. Molecular basis of wax-
702 based color change and UV reflection in dragonflies. *Elife*. **8**, e43045 (2019).
- 703 28. H. T. Ghiradella, M. W. Butler. Many variations on a few themes: a broader look at
704 development of iridescent scales (and feathers). *J. Royal Soc. Interface*. Apr **6**, S243-
705 51 (2009).
- 706 29. R. D. Reed. Evidence for Notch-mediated lateral inhibition in organizing butterfly
707 wing scales. *Development Genes and Evolution*. **214**, 43-6 (2004).
- 708 30. R. Galant, J. B. Skeath, S. Paddock, D. L. Lewis, S. B. Carroll. Expression pattern of
709 a butterfly achaete-scute homolog reveals the homology of butterfly wing scales and
710 insect sensory bristles. *Current Biology*. **8**, 807-13 (1998).
- 711 31. I. G. Tilney, P. S. Connelly, K. A. Vranich, M. K. Shaw, G. M. Guild. Actin filaments
712 and microtubules play different roles during bristle elongation in *Drosophila*. *J. Cell*.
713 *Sci*. **113**, 1255-65 (2000).
- 714 32. S. Djokic, B. Anna, I. Zurim, N. Urakova, J. Ragson, U. Abdu. Actin bundles play
715 different role in shaping scale as compare to bristle in mosquito *Aedes aegypti*.
716 *bioRxiv*. doi: <https://doi.org/10.1101/2020.04.06.027110> (2020).
- 717 33. I. Overton. Microtubules and microfibrils in morphogenesis of the scale cells of
718 *Ephestia kuhniella*. *J. cell biology*. **29**, 293-305 (1966).
- 719 34. A. Bitan, G. M. Guild, D. Bar-Dubin, U. Abdu. Asymmetric microtubule function is
720 an essential requirement for polarized organization of the *Drosophila* bristle. *Molec*.
721 *cell. biol*. **30**, 496-507 (2010).
- 722 35. A. Bitan, I. Rosenbaum, U. Abdu. Stable and dynamic microtubules coordinately
723 determine and maintain *Drosophila* bristle shape. *Development*. **139**, 1987-96 (2012).

- 724 36. G. Gemne. Ontogenesis of corneal surface ultrastructure in nocturnal Lepidoptera.
725 *Philosophical Transactions of the Royal Society of London. B, Biological Sciences.*
726 **262**, 343-63 (1971).
- 727 37. A. Fröhlich. A scanning electron-microscopic study of apical contacts in the eye
728 during postembryonic development of *Drosophila melanogaster*. *Cell and tissue*
729 *research.* **303**, 117-28 (2001).
- 730 38. M. Kryuchkov, A. Blagodatski, V. Cherepanov, V. L. Katanaev. “Arthropod corneal
731 nanocoatings: diversity, mechanisms, and functions” in *Functional Surfaces in*
732 *Biology III.* (Springer, Cham, Switzerland, 2017), pp. 29-52.
- 733 39. B. Moussian. Recent advances in understanding mechanisms of insect cuticle
734 differentiation. *Insect biochem. molec. biol.* **40**, 363-75 (2010).
- 735 40. A. G. Gibbs. Water-proofing properties of cuticular lipids. *American Zoologist.* **38**,
736 471-82 (1998).
- 737 41. I. Román-Kustas, J. B. Hoffman, J. H. Reed, A. E. Gonsalves, J. Oh, L. Li, S. Hong,
738 K. D. Jo, C. E. Dana, N. Miljkovic, D. M. Crokek. Molecular and Topographical
739 Organization: Influence on Cicada Wing Wettability and Bactericidal Properties.
740 *Advanced Materials Interfaces.* **7**, 2000112 (2020).
- 741 42. A. P. Ivanova, S. H. Nguyen, H. K. Webb, J. Hasan, V. K. Truong, R. N. Lamb, X.
742 Duan, M. J. Tobin, P. J. Mahon, R. J. Crawford. Molecular organization of the
743 nanoscale surface structures of the dragonfly *Hemianax papuensis* wing epicuticle.
744 *PLoS One.* **8**, e67893. (2013).
- 745 43. A. Shevtsova, C. Hansson, D. H. Janzen, J. Kjærandsen. Stable structural color
746 patterns displayed on transparent insect wings. *Proc. Natl. Acad. Sci.* **108**, 668-73
747 (2011).
- 748 44. D. G. Stavenga. Thin film and multilayer optics cause structural colors of many
749 insects and birds. *Materials Today: Proceedings.* **1**, 109-21 (2014).
- 750 45. A. Gorb, S. Böhm, N. Jacky, L. P. Maier, K. Dening, S. Pechook, B. Pokroy, S. Gorb.
751 Insect attachment on crystalline bioinspired wax surfaces formed by alkanes of
752 varying chain lengths. *Beilstein J. Nanotech.* **5**, 1031-41 (2014).
- 753 46. R. H. Siddique, S. Vignolini, C. Bartels, I. Wacker, H. Hölscher. Colour formation on
754 the wings of the butterfly *Hypolimnas salmacis* by scale stacking. *Scientific reports.*
755 **6**, 36204 (2016).
- 756 47. I. R. Hooper, P. Vukusic, R. J. Wootton. Detailed optical study of the transparent
757 wing membranes of the dragonfly *Aeshna cyanea*. *Optics express.* **14**, 4891-7 (2006).

758 **Acknowledgments**

759 We would like to thank the Angie Serrano, Paola Betucci, Idoia Quintana-Urzainqui and
760 Helena Bilandzija from the MBL Embryology Course and Cao Lu Yan from the MBL
761 Physiology Course for their preliminary work on scale morphology of clearwing
762 Lepidoptera, and subsequent work by Jaap van Krugten, Raymundo Picos, and Johnny
763 On at UC Berkeley. We also thank Rachel Thayer, Arnaud Martin, Damien Gailly,
764 Melanie McClure, Luca Livraghi, Oscar Paneso, Rémi Mauxion and Owen McMillan for
765 their assistance with fieldwork, rearing, and preliminary experiments. We thank Fred
766 Gagnon of Magic Wings Butterfly Conservatory and Gardens for assistance with butterfly
767 rearing and Neil Tsutsui for support with the GC-MS experiments. Members of the Patel
768 Lab, Craig Miller, and Noah Whiteman provided helpful feedback on the manuscript.
769 RHS acknowledges the support from the Beckman Institute of the California Institute of
770 Technology to the Molecular Materials Research Center. **Funding:** This work was
771 supported by a grant from the Human Frontier Science Program (RGP0014/2016), a
772 France-Berkeley fund grant (FBF #2015--58) and an ANR grant (CLEARWING project,
773 ANR-16-CE02-0012). **Author contributions:** Conceived and designed the experiments:
774 AFP and NHP. Performed the experiments: AFP, RHS, EIC, KH. All authors contributed
775 to analysis of the results, contributed reagents/materials/analysis tools and contributed to
776 writing the paper. **Competing interests:** The authors declare they have no competing
777 interests.

778

779

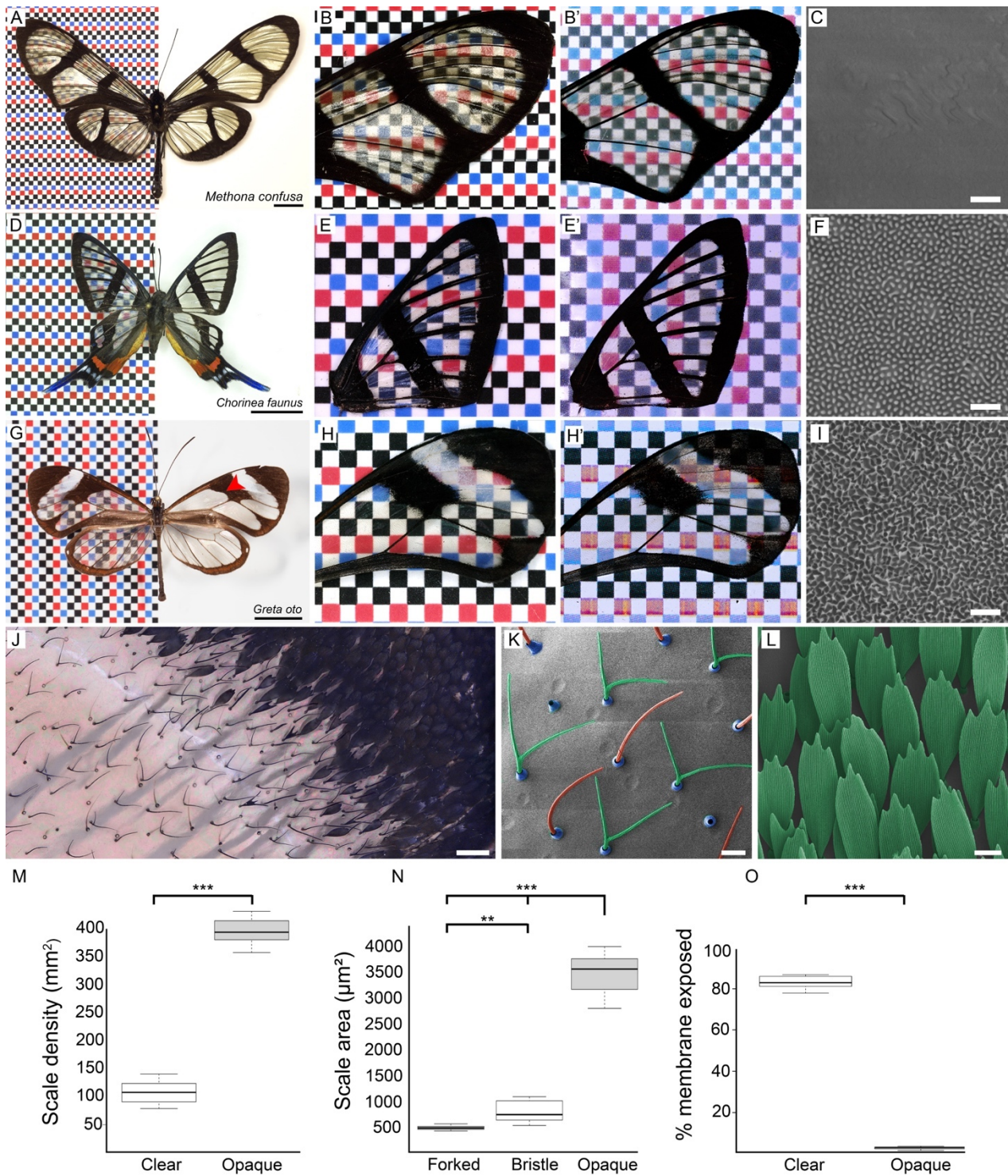
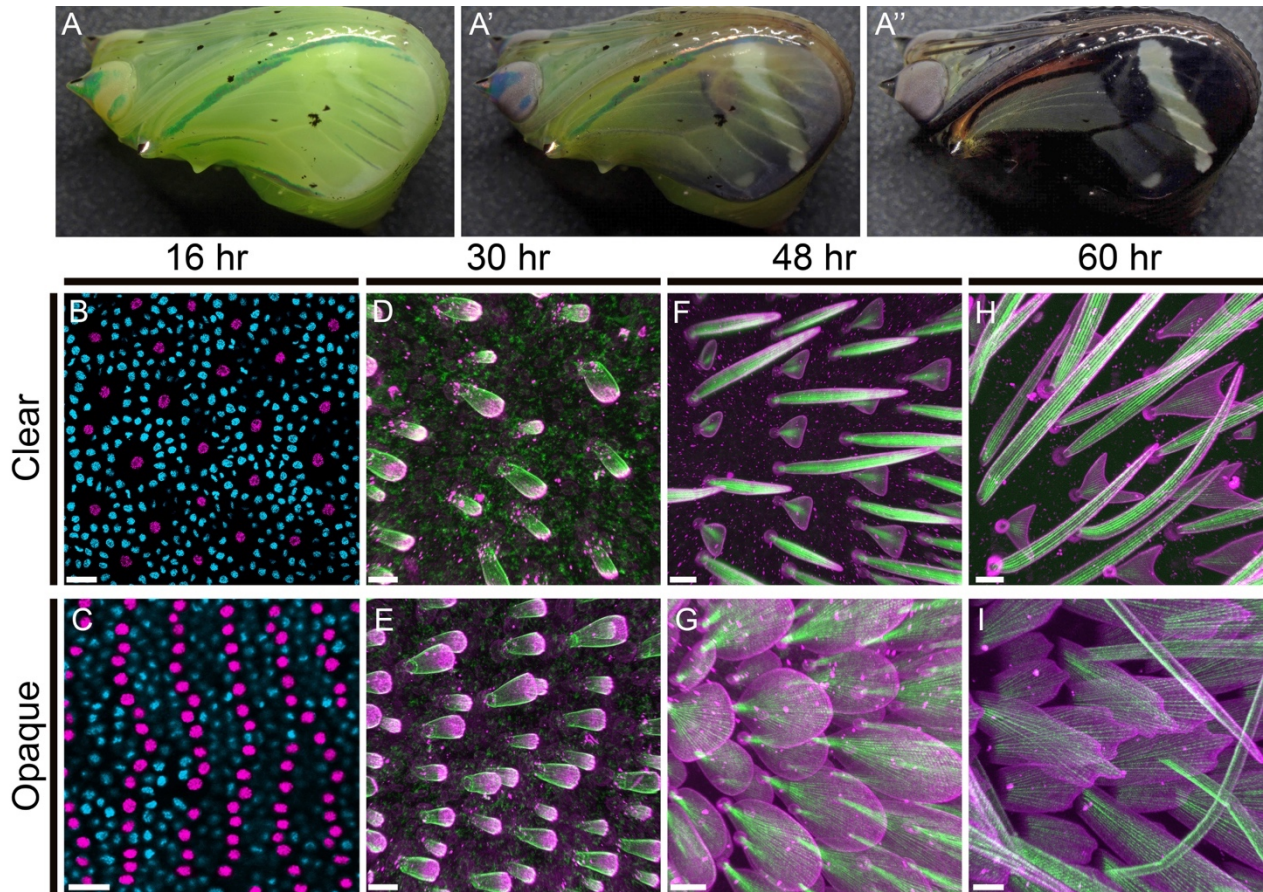


Fig. 1. Examples of clearwing butterflies and wing scale features in *Greta oto*

(A) Giant glasswing *Methona confusa* (Nymphalidae: Ithomiini). Scale bar = 1 cm. Wings under (B) reflected and (B') transmitted light illustrating general transparency, but strong light reflectance off the wing surface in this species. (C)

785 The surface of the wing membrane is smooth and devoid of nanostructures. Scale
786 bar = 1 μm . **(D)** Longtail glasswing *Chorinea faunus* (Riodinidae). Scale bar = 1
787 cm. Wings under **(E)** reflected and **(E')** transmitted light illustrating minimal
788 reflectance. **(F)** The membrane surface contains dome-shaped chitin
789 nanoprotuberances that generate anti-reflective properties (21). Scale bar = 1 μm .
790 **(G)** Glasswing *Greta oto* (Nymphalidae: Ithomiini). Red arrowhead indicates the
791 representative clear and opaque wing region investigated, scale bar = 1 cm. Wings
792 under **(H)** reflected and **(H')** transmitted light illustrating minimal reflectance. **(I)**
793 The surface of the wing membrane contains irregularly sized nanopillars that
794 enable omnidirectional anti-reflective properties (10). Scale bar = 1 μm . **(J)** High
795 magnification of a transition boundary between a clear (left side) and opaque
796 (upper right side) wing region in *G. oto*. Scale bar = 100 μm . **(K)** SEM of adult
797 scales in a clear wing region of *G. oto*, revealing the alternating forked (green
798 false coloring) and bristle-like (red false coloring) scale morphologies (socket
799 false colored in blue). Scale bar = 20 μm . **(L)** SEM of scales in an opaque wing
800 region in *G. oto*, highlighting typical large, flat scale morphologies. Scale bar = 20
801 μm . **(M)** Measurements of scale density in clear and opaque wing regions, **(N)**
802 scale surface area for forked, bristle-like, and opaque scale morphologies, and **(O)**
803 percent of wing membrane exposed in *G. oto* clear and opaque regions. Error bars
804 indicate means + SD of four measurements taken from wings in three different
805 individuals, P-values are based on Student's t-test for **(M)**, **(O)**, and ANOVA test
806 for **(N)**, ***P < 0.001; **P < 0.01.

807



808

809

810

Fig. 2. Pupal wing development and cytoskeletal organization of scales in clear and opaque regions

811

(A) Representative image of a *Greta oto* pupa ~5 days after pupal formation

812

(APF), (A'-A'') developing up to the melanic stage ~7 days APF, just prior to

813

eclosion. (B) Early wing development 16 hours APF stained with DAPI (nuclei)

814

in a clear wing region and (C) opaque wing region. The clear region contains a

815

reduced number of sensory organ precursor (SOP) cells (which are the precursor

816

cells to the scale and socket cells) relative to the opaque region. Scale bar = 20

817

µm. SOP cells are false colored magenta for better viewing. Simultaneous

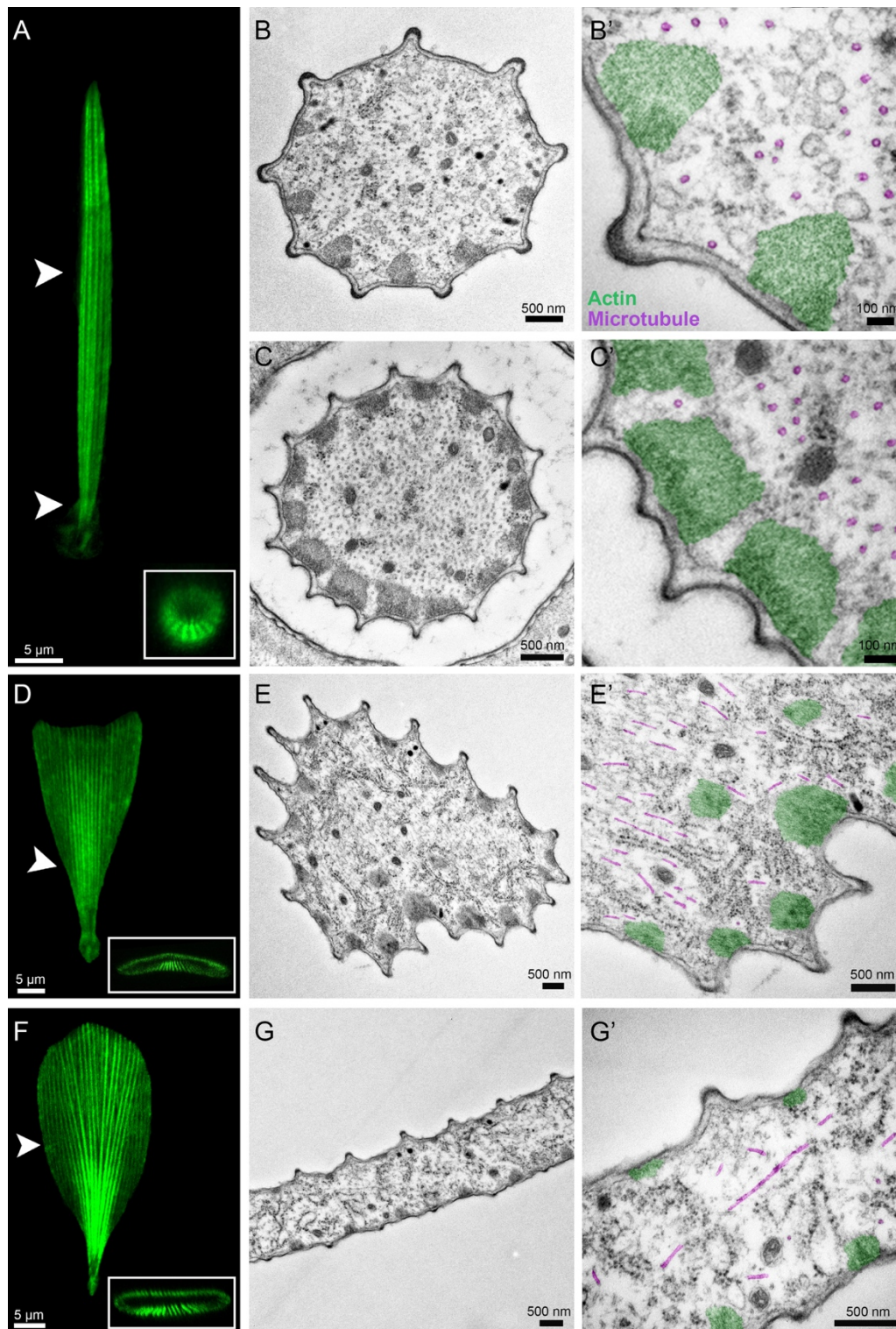
818

confocal imaging of fluorescently labeled scale cell membrane (wheat germ

819

agglutinin; WGA, magenta), and F-actin (phalloidin, green), comparing clear

820 wing regions **(D, F, H)** to opaque wing regions **(E, G, I)**. At 30 h APF **(D, E)**
821 WGA and phalloidin staining reveal early scale buds extending from the wing
822 epithelium. F-actin reveals loosely organized parallel actin filaments protruding
823 from the membrane. 48 h APF **(F, G)** scales have grown and changed in
824 morphology. Short actin filaments have reorganized and formed smaller numbers
825 of thick, regularly spaced parallel bundles under the surface of the cell membrane.
826 **(F)** In the clear wing region, scale cells alternate between triangular shapes and
827 bristles. 60 h APF **(H, I)**, developing scales have become more elongated. **(H)** The
828 triangular-shaped scales in the clear wing region have proceeded to generate two
829 new branches, which fork and elongate bidirectionally, while bristle-like scales
830 have rapidly elongated and curved. **(I)** In the opaque region, scales are longer,
831 wider, and have now developed serrations at the tips. Scale bar in **(D-I)** = 10 μm .



832

833

834

Fig. 3. Confocal and transmission electron microscopy transverse sections of developing bristle (top), forked (middle) and flat (bottom) scales 48 hours APF

835 (A) Confocal projection of a bristle-like scale morphology (phalloidin) in a clear
836 wing region. White arrowhead shows representative regions of transverse TEM
837 sections. Scale bar = 5 μm . TEM of a bristle-like scale in a distal region (B-B')
838 and a basal region near the socket cell (C-C'). Note the peripheral actin bundles
839 (false colored green) and internal microtubule rings (false colored magenta). The
840 more distal region of the scale (B) contains a lower density of microtubules
841 relative to the base of the scale (C). Scale bars in (B,C) = 500 nm and scale bars in
842 (B',C') = 100 nm. (D) Confocal projection of a developing forked scale
843 (phalloidin) in a clear wing region. White arrowhead shows representative regions
844 of transverse TEM sections. Scale bar = 5 μm . (E-E') TEM of a forked scale
845 reveals peripheral bundles of actin (false colored green), with thicker actin
846 bundles on the ventral side of the scale and internal microtubules (false colored
847 magenta). Two internal bundles of actin filaments can be observed in the
848 cytoplasm (E'). Scale bars in (E-E') = 500 nm. (F) Confocal projections of
849 developing flat, round scale (phalloidin) in an opaque wing region. White
850 arrowhead shows representative regions of transverse TEM sections. Scale bar = 5
851 μm . (G-G') TEM reveals asymmetry in the actin bundles (false colored green),
852 which are thicker on the bottom side of the scale relative to the upper surface.
853 Microtubules (false colored magenta) are found in various orientations. Scale bar
854 in (G-G') = 500 nm.

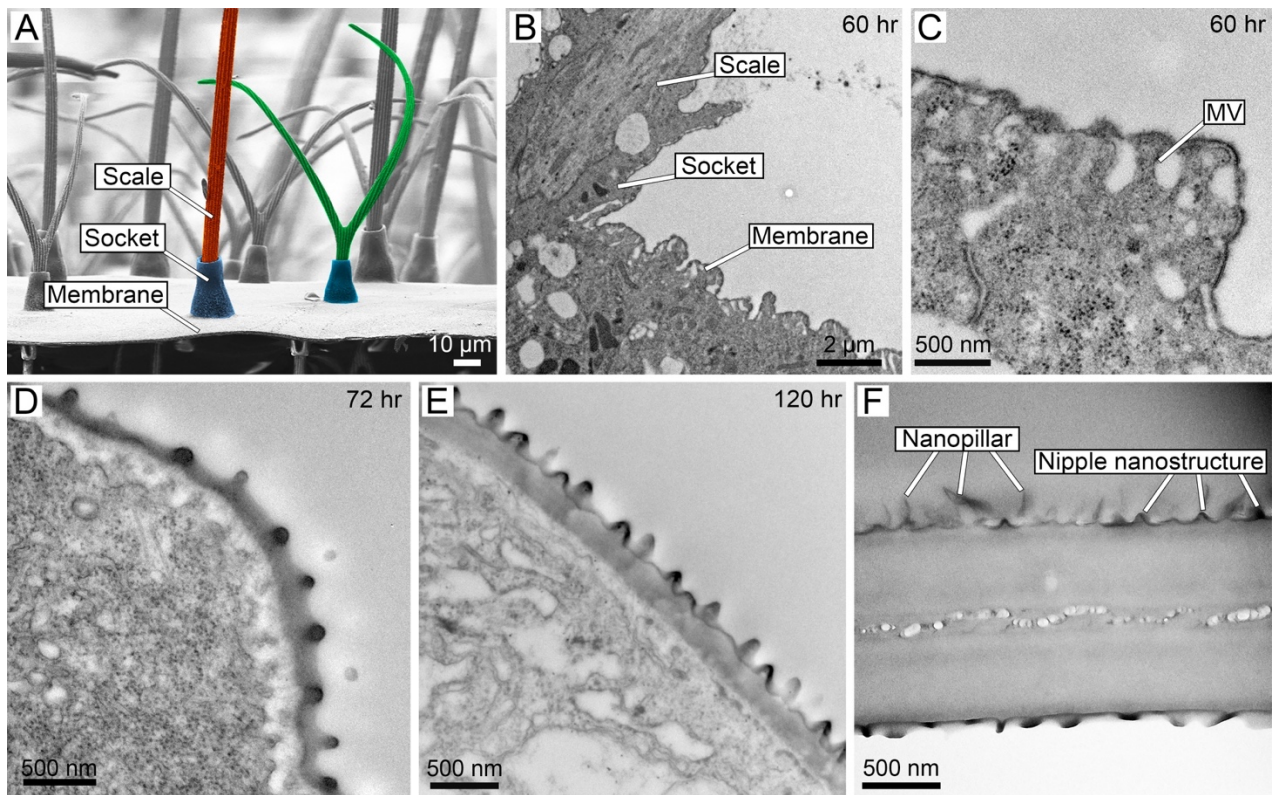


Fig. 4. Ontogeny of wing membrane surface nanostructures

(A) SEM cross section (side view) of an adult *Greta oto* clear wing region. Scale bar = 10 μm . Bristle-like scale false colored in red, forked scale false colored in green, sockets false colored in blue. (B) TEM transverse section of epithelial tissue 60 h APF, showing lateral scale growth and wing membrane cells. Scale bar = 2 μm . (C) Higher magnification of developing wing epithelial cells at 60 h APF show microvilli (MV) projections, which appear as slender linear extensions from the inner margins of the developing cells that insert into a thin layer of electron-dense material. Lamina evaginations appear in the section as domes. (D) TEM of epithical tissue 72 h APF and (E) 120 h APF shows wing surface nanostructures protruding from the surface, with tips of microvilli still attached to the inner surface of the wing membrane. (F) TEM of the adult wing membrane. The surface contains dome-shaped nipple nanostructures and an upper layer of nanopillars. Scale bar in (C-E) = 500 nm.

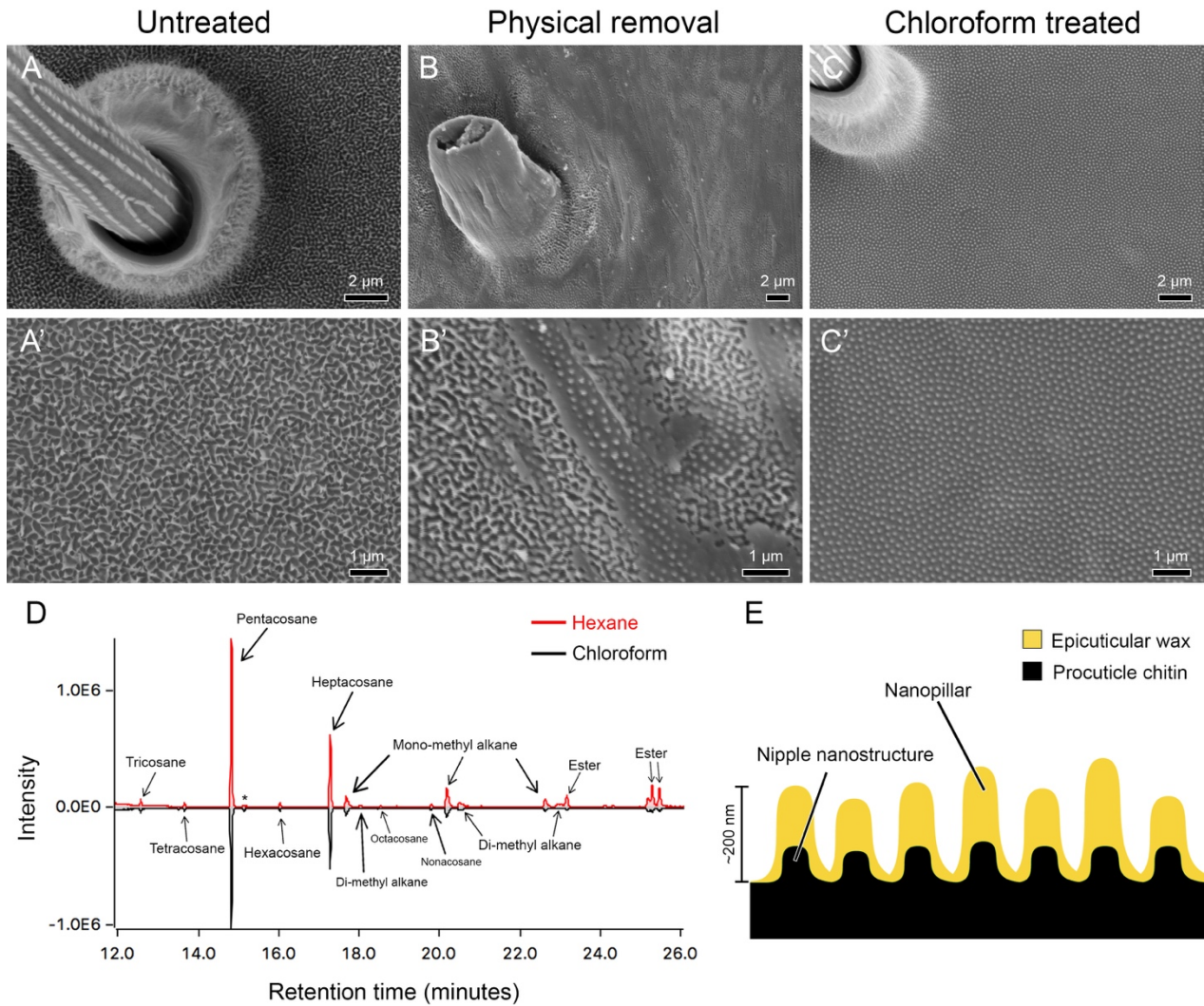
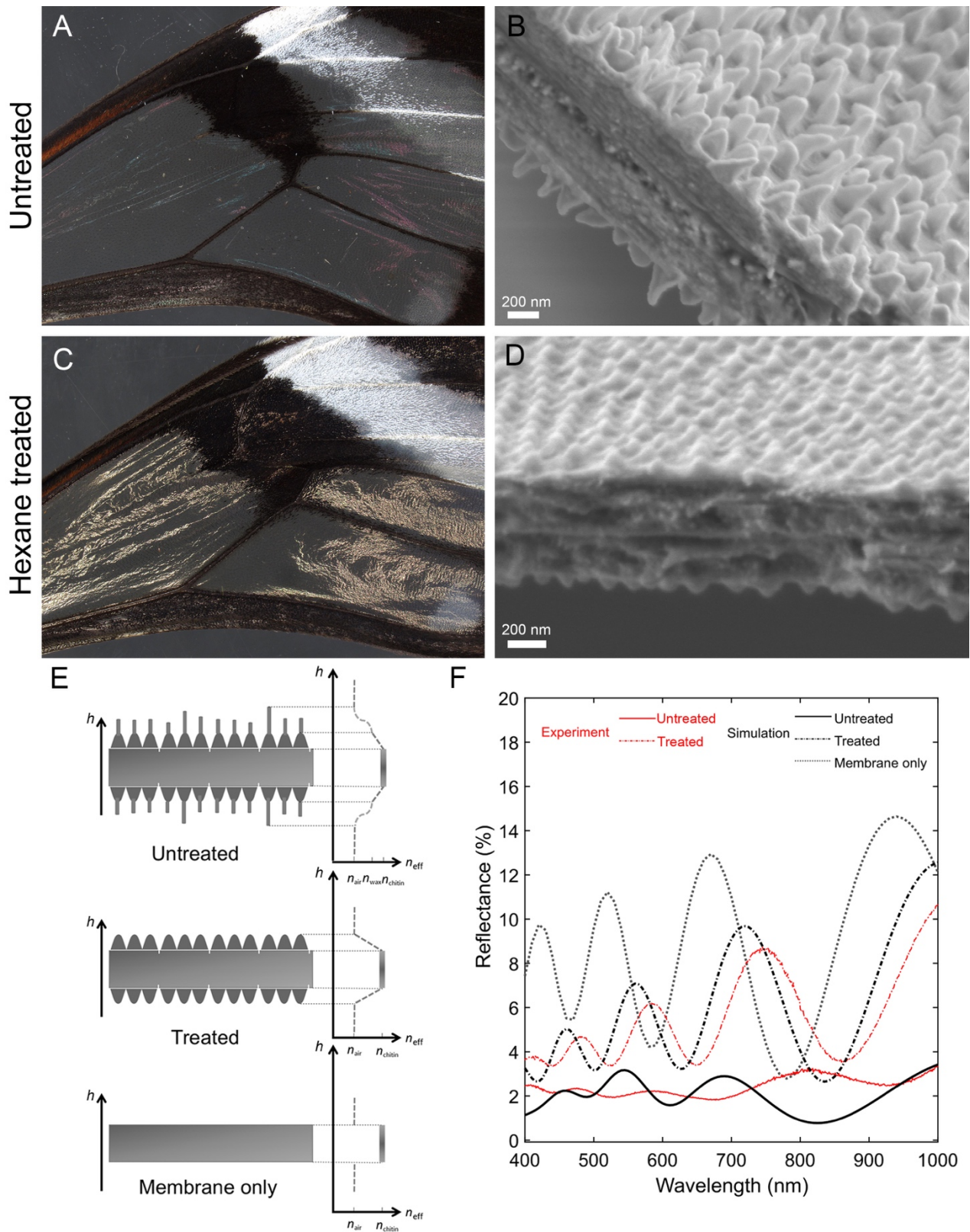


Fig. 5. Topographical organization and biochemical composition of wing surface nanostructures

Scanning electron microscopy of the transparent wing membrane surface of *Greta oto* under (A-A') untreated condition, highlighting the presence of irregularly arranged nanopillar structures covering the surface, (B-B') physical treated condition, revealing partial removal of surface nanopillars, and a lower layer of more regularly arranged nipple-like nanostructures and (C) chloroform treated condition, revealing complete removal of the upper layer of nanopillars, and remaining lower layer of nipple-like nanostructures. Scale bars in (A, B C) = 2 μm , scale bars in (A', B', C') = 1 μm . (D)

879 Chromatogram of hexane-treated (top; red line) and chloroform-treated (bottom; black
880 line) clearwing extracts. X-axis shows the retention time in minutes and Y-axis shows the
881 abundance of total ion current. **(E)** Schematic of proposed wing surface membrane
882 nanostructures in *Greta oto*, composed of chitin-based procuticle and wax-based
883 epicuticle.



884

885

886

Fig. 6. Structural elements, reflectance spectra and optical modeling of anti-reflective nanostructures

887 Optical images and cross section scanning electron microscopy of *Greta oto* (**A, B**)
888 untreated wings, illustrating low reflectance and the presence of nanopillars on the wing
889 membrane surface and (**C, D**) hexane-treated wings illustrating increased reflectance and
890 the loss of nanopillars on the wing membrane, but presence of nipple-like nanostructures
891 on the surface. Scale bars for (**B, D**) = 200 nm. (**E**) Optical modeling of effective
892 refractive index conditions for untreated (top), with nanopillars of variable height together
893 with cuticle-based nipple nanostructures on the wing membrane, treated (middle) with
894 cuticle-based nipple nanostructures on wing membrane and wing membrane without any
895 nanostructures (bottom). Y-axis represents height h and X-axis represents effective
896 refractive index condition of air (n_{air}), chitin (n_{chitin}), and wax (n_{wax}). (**F**) Representative
897 reflectance spectra of experimental (red) and simulation data (black) for untreated wings
898 with nanopillars on the membrane surface (solid line), hexane-treated wings with the
899 wax-based layer of nanopillars removed (dashed line) and membrane only (dotted line).

900 **Supplementary Materials**

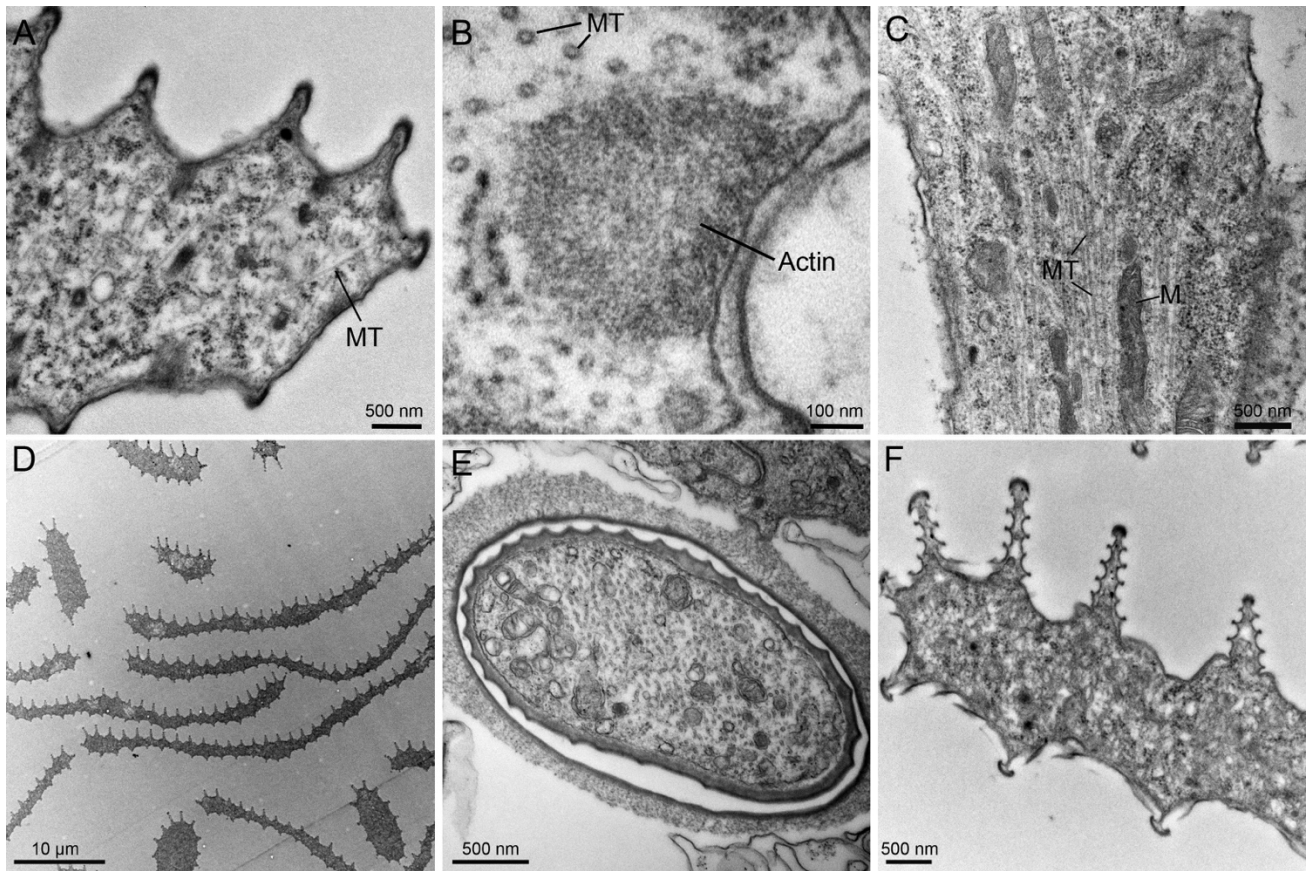
901 **Table S1. GC-MS relative proportions (mean \pm standard deviation) of wing**
902 **cuticular compounds isolated from *Greta oto*.**

903

904 **Table S2. Spectrometry of *Greta oto* untreated and hexane treated clear wing**
905 **regions and simulated reflectance spectra.**

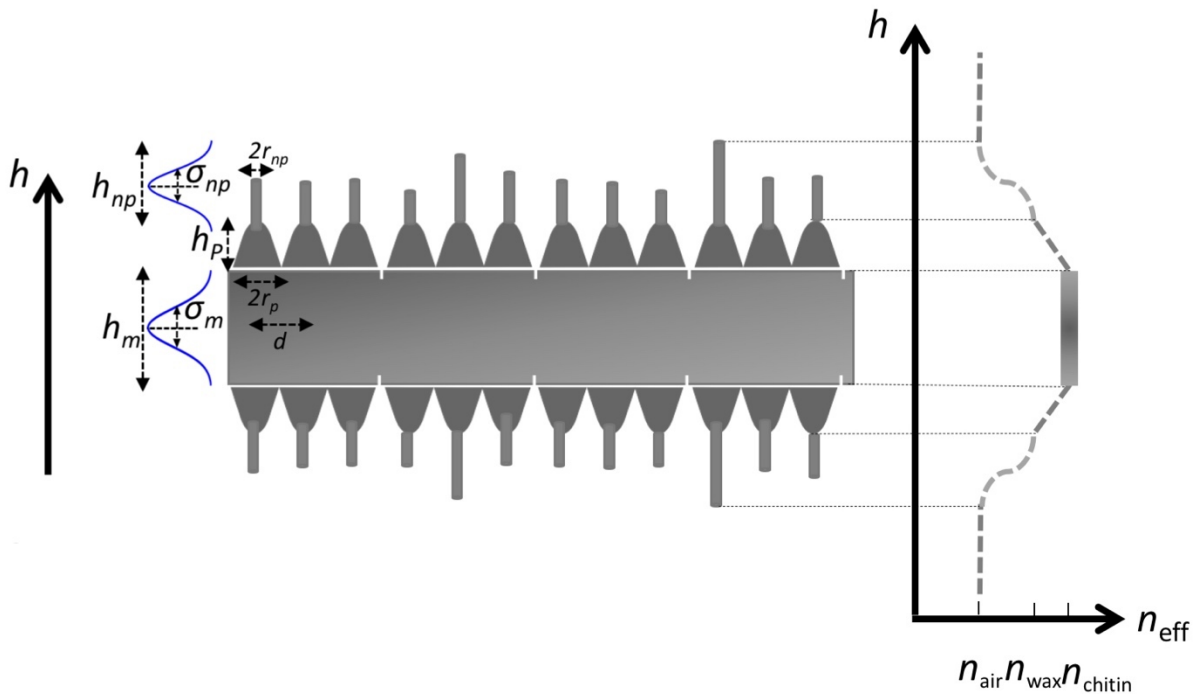
906

907 **Movie S1. 3D projection of developing scales in a clear wing region 48 hours after**
908 **pupal formation.** 3D projection and rotation of the same scales shown in Fig. 2F, 48
909 hours APF in a clear wing region. WGA (magenta) stains cell membranes and phalloidin
910 (green) stains F-actin and DAPI (blue) stains nuclei. Short actin filaments have
911 reorganized and formed smaller numbers of thick, regularly spaced parallel bundles just
912 under the surface of the cell membrane. Scales alternate with future forked scales
913 appearing as triangular shapes and longer future bristle-like shapes.



914
915 **Fig. S1. TEM micrographs of scales 72 hours (top) and 120 hours (bottom) after**
916 **pupal formation**

917 (A) TEM micrograph of a developing opaque scale 72 h APF, highlighting microtubule
918 arrangement (MT). (B) Thick actin bundles contain dense, hexagonally packed F-actin
919 filaments. (C) Basal region of a developing scale outgrowth and socket cell. Developing
920 scales 72 h APF contain dense populations of microtubules (MT) and numerous internal
921 organelles, including mitochondria (M), electron dense vesicles and free single
922 ribosomes. (D) Transverse section of developing scales around 120 h APF, highlighting
923 both flat and thin, bristle-like scale morphologies. Cross section near the (E) base and (F)
924 distal region of scales 120 h APF, showing thickened cuticle and ridge morphologies.



925
926 **Fig. S2. Optical modeling parameters and effective refractive index condition for**
927 **untreated transparent wing of *Greta oto***

928 Schematic representation for the optical modeling parameters of wing membrane and
929 surface nanostructures. Average distance between two nanostructures represented as d ,
930 conical shaped cuticular nipple nanostructures height as h_p , wax-based irregular
931 nanopillars radius as r_{np} , mean height as h_{np} and variance σ_{np} , and membrane thickness as
932 h_m and variance σ_m . Y-axis represents height h and X-axis represents effective refractive
933 index condition of air (n_{air}), chitin (n_{chitin}), and wax (n_{wax}).

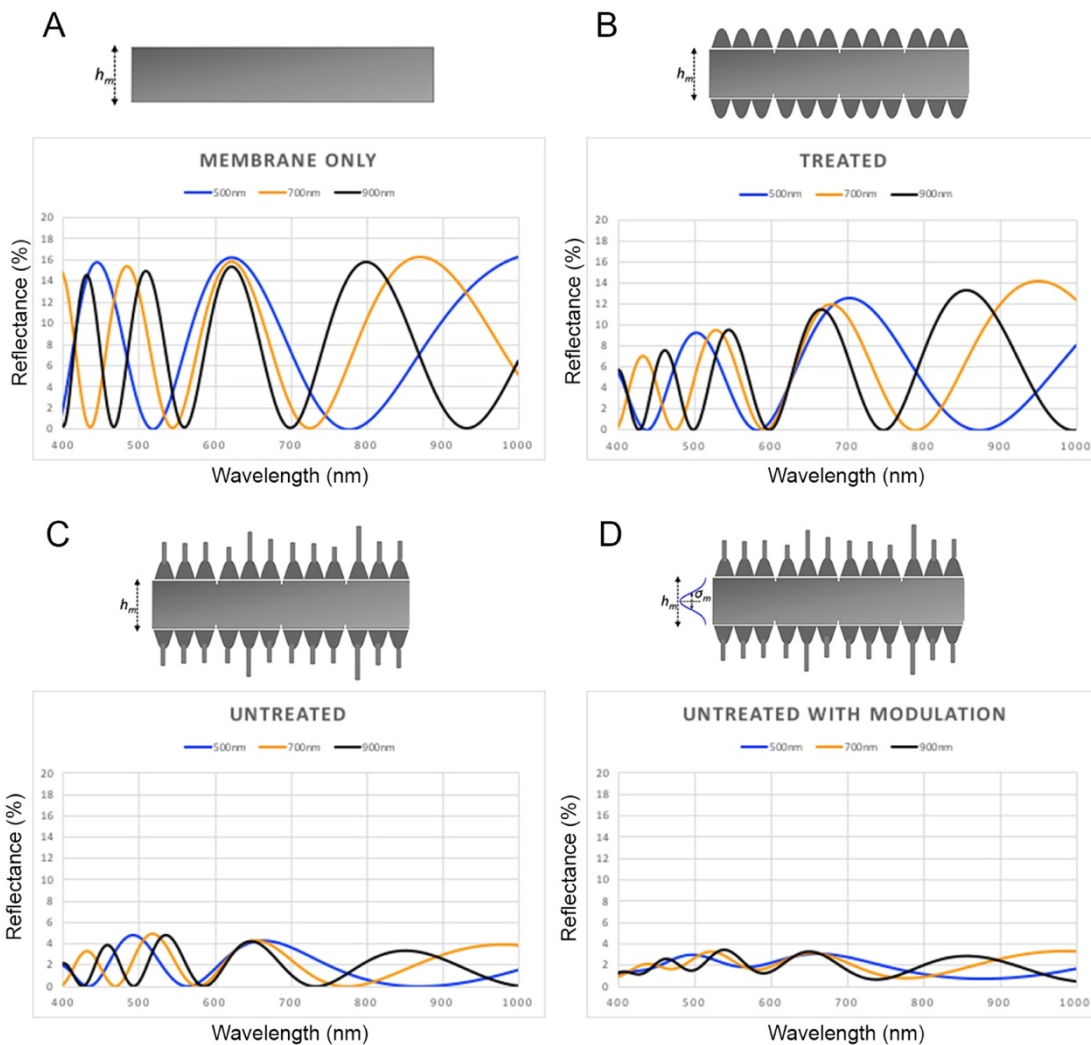


Fig. S3. Optical simulations for mean membrane thickness and modulation of thickness under different wing architecture models

Simulation reflectance spectra of (A) Membrane only (lacking surface nanostructures) with varying mean membrane thickness. (B) Treated wings (containing cuticle-based nipple nanostructures but lacking wax-based irregular nanopillars) with varying mean membrane thickness. (C) Untreated wings (containing wax-based irregular nanopillars and nipple nanostructures) with varying mean membrane thickness and no modulation in thickness. (D) Untreated wings with variable mean membrane thickness and modulation of 43 nm variance in thickness.